ADVANCED FUNCTIONAL MATERIALS
www.afm-journal.de

Check for updates

Sculpting Bio-Inspired Surface Textures: An Adhesive Janus Periosteum

Yuhe Yang, Tianpeng Xu, Ho Pan Bei, Yuanjin Zhao, and Xin Zhao**

Existing artificial periostea faces difficulty in supporting the entire bone repair cycle due to the absence of adhesion-centric design and effective cell manipulation, leading to poor inhibition of soft tissue infiltration and induction of osteogenesis and angiogenesis. Here, a Janus periosteum with interior surface adhesion and exterior anatomical patterns to mimic the structure and function of natural periosteum is presented. Photo-crosslinkable polymers are employed to replicate the exterior anisotropic surface structured microgrooves for cell fate manipulation and assemble gecko-inspired fibrillar setae arrays for interior surface adhesion. To further bolster its underwater adhesiveness, mussel-inspired poly (dopamine methacrylamide-co-hydroxyethyl methacrylate) (PDMH) is coated onto the periosteum surfaces. This periosteum presents adhesiveness with strong shear and normal adhesion in both dry and wet conditions due to the coordinated interactions of micro setae arrays and PDMH coating; it also boasts effective cell modulation for enhanced synchronous osteogenesis and angiogenesis, without the aid of growth factors. Moreover, the Janus periosteum is found to enhance bone regeneration in vivo with increased new bone formation and neovascularization. It is envisioned that this Janus periosteum will be able to streamline bone fracture surgical repair as a rapidly adhesive, low-maintenance yet robust bandage to significantly cut down the healing phase.

1. Introduction

Periosteum is a dense tissue membrane covering the exterior bone surface. Due to its osteogenic and angiogenic nature, periosteum has been considered critical to bone reconstruction.[1] Currently, artificial periosteum are mostly fabricated by cell sheets,[2] acellular dermis,[3] electrospun fibers,[4] and hydrogels;[5] however, these artificial periosteum require additional fixation during implantation due to their limited adhesiveness to the bone defect site, which may also compromise their functionality to inhibit the soft tissue ingrowth and prevent fracture wound from scar tissue formation.[1b] Moreover, most of these artificial periosteum fail to reflect the intrinsic biological function (e.g., osteogenesis and angiogenesis) of the natural periosteum. To enhance the osteogenesis and angiogenesis capability, direct incorporation of vulnerable biomolecules (e.g., growth factors) has been used;[5,6] nevertheless, the outcome of this strategy is not satisfactory due to the uncontrollable release and the possible side-effects (e.g., carcinogenicity). This calls for artificial periosteum with strong tissue adhesion to avoid fixation procedure and prevent scar tissue ingrowth, as well as synchronous osteogenesis and angiogenesis potential with no involvement of fragile biomacromolecules, for enhanced bone regeneration.

Previously, our group has developed fluid, photo-crosslinkable poly (lactide-co-propylene glycol-co-lactide) dimethacrylates (PGLADMA).[7] This polymer is initially fluid and can be solidified upon light exposure for a few seconds. Moreover, the crosslinked PGLADMA demonstrates excellent mechanical property (Young's modulus ≈ 19 MPa) and non-swelling after water immersion, which allows for fabrication of sophisticated structures. Plus its biocompatibility, PGLADMA is more superior in terms of fabrication of artificial periosteum compared to poly(ethylene glycol) diacrylate or gelatin methacryloyl hydrogels. Here, we sculpt the materials with delicate surface textures to construct an adhesive Janus periosteum (**Figure 1**). We first molded fibrillar arrays (2 µm in diameter and 4 µm in height) mimicking gecko feet pad on one side of the Janus periosteum for tissue adhesiveness. This fibrillar array dimension has proven capability to generate strong friction and adhesion force with surrounding tissues.[8] We then carved microgrooved patterns (with 40, 80, and 120 µm interval) resembling the

Dr. Y. Yang, T. Xu, H. P. Bei, Dr. X. Zhao
Department of Biomedical Engineering
The Hong Kong Polytechnic University
Hong Kong 999077, China
E-mail: xin.zhao@polyu.edu.hk
T. Xu
Orthopedics and Sports Medicine Center
The Affiliated Suzhou Hospital of Nanjing Medical University
Suzhou 215000, China
Prof. Y. Zhao
Department of Rheumatology and Immunology
The Affiliated Drum Tower Hospital of Nanjing University Medical School
Nanjing 210008, China
E-mail: yjzhao@seu.edu.cn
Prof. Y. Zhao
State Key Laboratory of Bioelectronics
School of Biological Science and Medical Engineering
Southeast University
Nanjing 210096, China

The ORCID identification number(s) for the author(s) of this article can be found under https://doi.org/10.1002/adfm.202104636.

DOI: 10.1002/adfm.202104636

 © 2021 Wiley-VCH GmbH

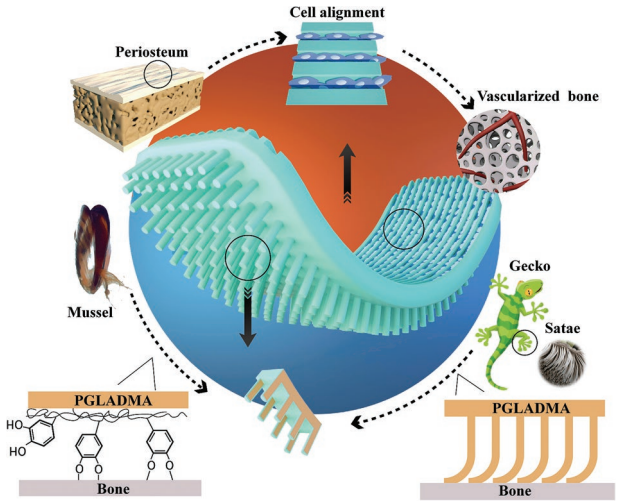

Figure 1. Schematic illustration of the bio-inspired Janus periosteum with anisotropic tissue adhesion and anatomical structure for bone regeneration. The periosteum is composed of mussel byssus inspired PDMH co-polymer coated PGLADMA matrix sculpted with gecko inspired fibrillar setae arrays and periosteum mimicking microgrooved patterns.

anatomically topographical surface texture of natural periosteum on the other side of the Janus periosteum. These microgrooved patterns have proven capability to stimulate osteogenesis and angiogenesis by modulating the cell morphology and cell focal adhesion (FA) without the aid of growth factors.[9] To further increase the tissue adhesiveness especially under physiological wet environments, we modified the periosteum surface by immobilizing the mussel-inspired catechol-rich poly (dopamine methacrylamide-co-hydroxyethyl methacrylate) (PDMH) co-polymer through one-step dip-coating.[10] The adhesive catechol group could form strong bonding with the tissue through the hydrogen bonding, π–π interactions and thiol reduction.[11] To the best of our knowledge, this is the first study to manipulate material surface structure to integrate strong tissue adhesion and effective cell fate regulation into one periosteum. Our adhesive Janus periosteum was found to tightly adhere to the natural bone under dry and wet conditions. Meanwhile, they could substantially promote osteogenesis and angiogenesis in vitro and in vivo. These unique features make our adhesive Janus periosteum highly desirable for bone regeneration and endow it with great clinical therapeutic efficacy.

2. Results and Discussion

We synthesized PGLADMA monomer as the matrix materials of the Janus periosteum. This is due to its fluidity and photo-crosslinkability which allows for creation of sophisticated surface structure. Fourier-transform infrared spectroscopy (FTIR) was performed to characterize the synthesized PGLADAM (Figure S1, Supporting Information). The peak at 1190 cm^{-1} of polypropylene glycol (PPG) corresponded to the "C—O—C" stretches, the peak at 1747 cm^{-1} of poly (lactide-co-propylene glycol-co-lactide) (PGLA) corresponded to "C=O" stretches which indicated the attachment of the lactide (LA) to PPG. In the spectra of PGLADMA, there was an additional peak at 1640 cm^{-1} due to "CC" stretches of the methacrylate groups in the final product. The above results confirmed the successful synthesis of PGLADMA.

We also used FTIR to characterize the PDMH synthesis (Figure S2, Supporting Information). The peak at 1290 cm^{-1} in dopamine methacrylamide (DMA) and PDMH corresponded to the phenolic "C—O—H" stretching of the catechol groups and the peaks at 1400–1600 cm^{-1} corresponded to the benzene skeleton. The disappearance of the peak at 1640 cm^{-1} in hydroxyethyl methacrylate (HEMA) and DMA indicated an efficient polymerization. Besides, the new peak at 1650 cm^{-1} corresponded to the "C=O" stretching of amide in PDMH, which further confirmed the chemical structure of the PDMH.[10b,12]

We then fabricated the adhesive Janus periosteum made of PGLADMA using photo-crosslinking-assisted injection molding and PDMH dip-coating (**Figure 2**A). To evaluate the structure integrity of the fabricated adhesive Janus periosteum, we examined the morphology of the PGLADMA-PDMH surfaces using scanning electron microscopy (SEM). We found that the exterior of the adhesive Janus periosteum was carved with precise microgrooves at 40, 80, or 120 µm intervals (Figure 2B–D) and the other surface was covered with gecko feet pad like fibrillar setae arrays (2 µm in diameter and 4 µm in height) (Figure 2E). Such high-resolution structure could be attributed to the excellent moldability of the PGLADMA polymer and indicated that the coating process has no detrimental effect on the surface structure. Besides, the cross sectioned images further demonstrated the anisotropic nature of the adhesive Janus periosteum (Figure S3, Supporting Information).

To evaluate the success immobilization of PDMH on the PGLADMA surfaces, we then investigated the chemical compositions of the PGLADMA surfaces using X-ray photoelectron spectroscopy (XPS) (Figure 2F). The appearance of the N 1s at about 400 eV could be observed in all PDMH coating samples and with the increase of the PDMH concentration from 1 to 5 mg mL^{-1}, the signal intensity of the N 1s increased. These results confirmed that the PDMH could be immobilized onto the PGLADMA surfaces, and the coating amount could be simply modulated by the PDMH concentration, which enables the precise modulation of adhesive strength by PDMH coating.

On the account of the successful fabrication of the adhesive Janus periosteum, we then moved to the evaluation of the adhesiveness of the periosteum. Ideally, the artificial periosteum should stably adhere to the defect site and withstand the pressure from the body fluids in both shear and normal directions to avoid rupture or detachment post-implantation. Such adhesiveness could therefore inhibit the possible osteolytic zone and bone resorption. The shear and normal tissue adhesion strength of our periosteum in dry and wet conditions were assessed as illustrated in **Figure 3**A. Under dry condition, we found that either the gecko inspired pattern (GP) or the mussel inspired adhesive PDMH coating could significantly increase the shear and normal adhesion strength due to the exploitation of van der Waals or the catechol-rich surface chemical structure.[13] The strongest adhesion could be achieved when both designs were combined because of the coordinated interfacial friction and bonding. The shear and normal adhesion strength of the GP-PDMH-5 group exhibited 3.6 and 2.8 N cm^{-2}, which was comparable with the previous studies (Figure 3C).[14] To

© 2021 Wiley-VCH GmbH

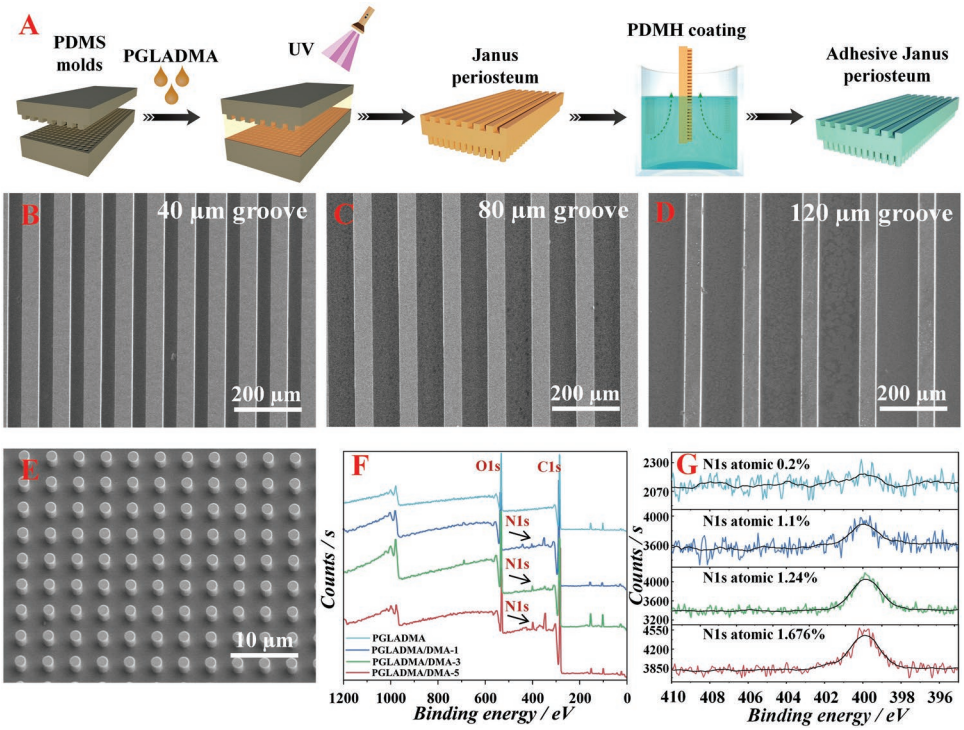

Figure 2. Fabrication and characterization of the adhesive Janus periosteum. A) Schematic diagram depicting the photo-crosslinking-assisted injection molding technique to fabricate the Janus periosteum. SEM images of the adhesive Janus periosteum including microgroove-patterned surface with different microgroove width of B) 40, C) 80, and D) 120 μm and E) fibrillar arrays on the adhesion surface. F) XPS spectra and G) N 1s XPS spectra of the naked PGLADMA and PDMH-coated PGLADMA with varying PDMH concentrations. The PGLADMA, PGLADMA/DMA-1, PGLADMA/DMA-3, and PGLADMA/DMA-5 denoted the naked Janus periosteum and the Janus periosteum with 1, 3, and 5 mg mL^{-1} PDMH coating, respectively. The magnified image is the high-resolution N1s XPS spectra of the coatings.

provide an index for the application of the Janus periosteum under physiological wet condition, we also evaluated the shear and normal adhesion strength under water. As expected, the PDMH coating exhibited improved water-resistant capacity compared to the GP structures; however, it was still observed that the combination of the GP structures and the PDMH coating could generate stronger adhesion underwater as the GP/PDMH-5 group presented 1.9 and 1.6 N cm^{-2} of the shear and normal adhesion strength (Figure 3D). Additionally, the application of the adhesive Janus periosteum to fresh bone could withstand 800 g weight (Figure 3B). These results demonstrated our adhesive Janus periosteum embodied robust dry and wet adhesion in their respective applications.

With adhesive properties of our Janus periosteum established, we proceeded to the evaluation of their biocompatibility in which the rat mesenchymal stem cells (rMSCs) were used as a model cell since it is highly relevant to bone defect regeneration.[15] We seeded the rMSCs onto the periosteum with different PDMH coating concentration to evaluate its effect on the cell behaviors. We found all materials groups can favorably support rMSC survival, adhesion, and proliferation with over 90% viability (**Figure 4**A–D). After the PDMH coating, the PGLADMA/PDMH groups demonstrated obvious pseudopodia shape on the surfaces with significantly increased cell spreading area compared to the naked PGLADMA group (Figure 4D). Besides, the quantitative analysis of cell proliferation also presented that the PDMH coating could substantially increase cell proliferation with PGLADMA/PDMH-5 groups showing the highest proliferation rate (Figure 4E). This may be attributed to the bioactive protein adsorption as evidenced in Figure S4, Supporting Information during cell culture. All in all, the above results indicated that our Janus periosteum embodied superior bone tissue adhesiveness and excellent biocompatibility in bone regeneration.

In our designed Janus periosteum, we aim to modulate the cell behaviors though the biomimicking microgrooved patterns We therefore evaluated the effect of the microgrooved patterns on the in vitro osteogenesis and angiogenesis, which is the major function of periosteum. We adopted the PGLADMA/PDMH-5 groups which presented the best capacity to promote cell adhesion with microgrooved topological structure to create biophysical cues to regulate cell behaviors. Here, we selected rMSCs and human umbilical vein endothelial cells (HUVECs) to evaluate the induced osteogenesis and angiogenesis.[1a,9b] As shown in **Figure 5**A,E, both the rMSCs and HUVECs presented oriented arrangement with *F*-actin assembled in the direction parallel with the patterns after three days of incubation. In contrast, the cells on the flat surface demonstrated a random arrangement without any skeleton orientation. Statistical analysis was also carried out to quantify the cell alignment. Approximate 65% and 46% of the rMSCs in 40 and 80 μm microgrooved patterns were rearranged in the 0°–10°; however, the cell alignment drastically decreased in the 120 μm microgrooved pattern. Similarly, the 40 μm microgrooved pattern

© 2021 Wiley-VCH GmbH

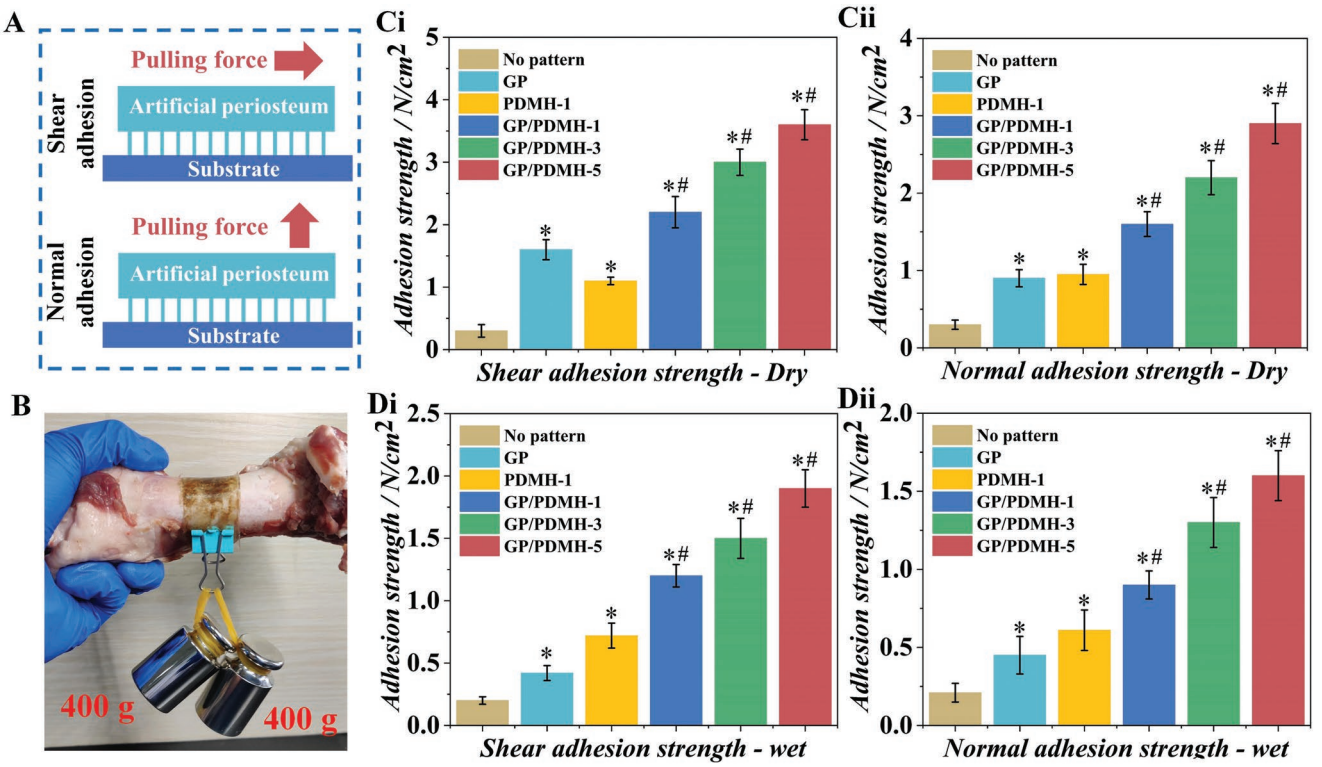

Figure 3. Characterization of the adhesion strength of the Janus periosteum. A) Schematic diagram showing the testing protocol of the shear and normal adhesion strength. B) Application of the anisotropic periosteum to fresh bone, which could withstand a 800 g weight. C) Quantification of the shear (Ci) and normal (Cii) adhesion strength under dry condition. D) Quantification of the shear (Di) and normal (Dii) adhesion strength under wet condition. GP referred to the naked gecko inspired adhesion surface, PDMH-1 referred to the no pattern surface with 1 mg mL^{-1} PDMH coating, and the GP-PDMH-1, GP-PDMH-3, and GP-PDMH-5 referred to the GP surface with 1, 3, and 5 mg mL^{-1} PDMH coating, respectively. $^{*}p < 0.05$ and $^{\#}p < 0.05$ were compared with the no pattern and GP group, respectively.

also presented the best orientation effect of HUVECs with 61% HUVECs were rearranged in the 0°–10° (Figure 5B,F). Our results agreed with the former literature that patterns with narrow widths could be beneficial for cell alignment.[16] Intriguingly, after 3 and 7 days of incubation, we found that the early osteogenic marker of alkaline phosphatase (ALP) activity were drastically promoted in the 40 µm microgrooved pattern groups compared to the flat surface (Figure 5C). We then used the quantitative reverse transcription-polymerase chain reaction (qRT-PCR) to examine the relative expression of the osteocalcin (OCN) protein, which is often used as a marker for the bone formation process. Our result indicated the relative expression of the OCN was substantially increased compared to flat surface which was in well agreement of the ALP activity analysis (Figure 5D).

Encouraged by the osteogenesis results, we then used the qRT-PCR to study the relative expression of the angiogenic genes of the HUVECs including vascular endothelial growth factor A (VEGF-A) and endothelial nitric oxide synthase (eNOS). We found the 40 µm microgrooved pattern exhibited substantial promotion of both VEGF-A and the eNOS gene expression, indicating that the highly longitudinally oriented HUVECs in 40 µm microgrooved pattern could present superior angiogenic potential (Figure 5G,H). These results could be attributed to the transmitting contraction stresses and mechanically balanced structure in the alignment morphology.[9c,17] To sum up, our results suggested that the periosteum-mimicking microgrooved pattern could be a promising tool for synchronous modulation of osteogenesis and angiogenesis for enhanced bone regeneration.

While previous characterizations were able to prove the effectiveness of our Janus periosteum in terms of adhesiveness and bioactivity under controlled environments, its long-term clinical relevance under physiological conditions remain unexplored. Hence, we used the rat critical-sized calvarial defect model to characterize the therapeutic performance of the Janus periosteum in vivo due to its superior repeatability, excellent cost effectiveness, and capacity for osteogenesis and angiogenesis evaluation (**Figure 6**B).[4,18] We prepared four kinds of periosteum: the membranes without any pattern in both surface (Flat–Flat group); the membranes with one gecko inspired surface and one naked surface (Flat–GP group); the membranes with one gecko inspired surface and one microgrooved surface (microgroove–GP group); the membranes with one gecko inspired surface and one microgrooved/PDMH coating surface (microgroove/PDMH–GP group). This grouping is to compare the effect of gecko feet pad structure, microgrooved pattern and the PDMH coating on the bone regeneration. Blank group without any implantation was used as control. Microcomputed tomography (micro-CT) was utilized to assess the macro bone regeneration after 4- and 8-week post-operation.[19] The new bone tissue could be observed in the defect site for

© 2021 Wiley-VCH GmbH

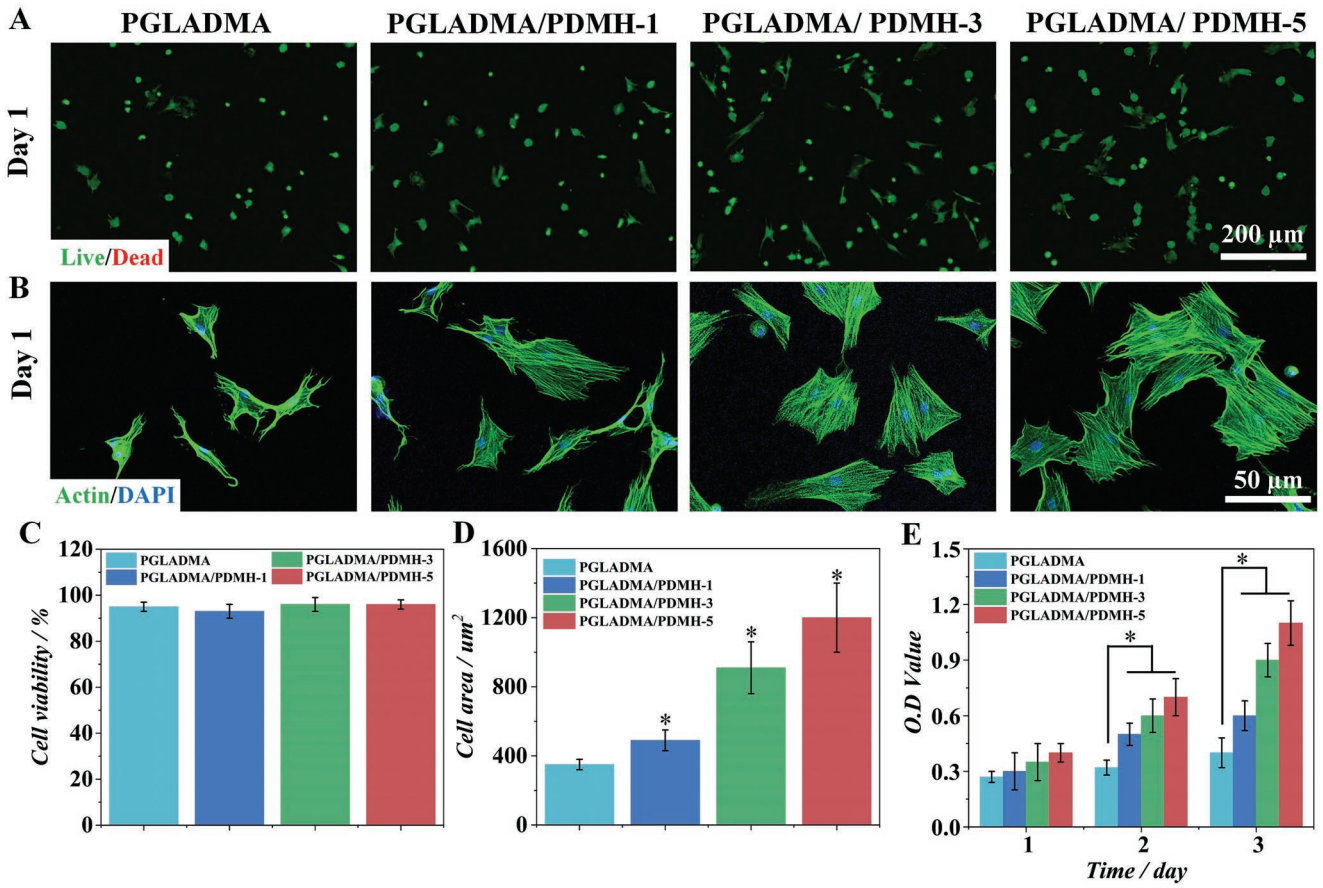

Figure 4. Biocompatibility of the Janus periosteum. A) Representative Live/Dead images of rMSCs on different Janus periosteum on day 1. Green and red fluorescence indicated viable and dead cells, respectively. B) Representative Actin/DAPI staining images of rMSCs on different Janus periosteum. Green and blue fluorescence indicated cell filaments and nuclei, respectively. Quantitative evaluation of C) cell viability and D) cell spreading area. E) Cell proliferation of rMSCs on different Janus periosteum measured using the MTT Cell Proliferation Kit. $^{*}p < 0.05$ compared with the naked PGLADMA group.

all experimental groups and the microgroove group presented significantly larger new bone area compared to the flat group, indicating such anatomical pattern could effectively promote the bone regeneration (Figure 6A). Moreover, the microgroove/PDMH group demonstrated the maximum new bone formation with highest bone mineral density (BMD) and bone tissue volume/total tissue volume (BV/TV) values, implying the synergistic influence of microgrooved patterns and the PDMH coating on accelerating bone regeneration (Figure 6C,D).

Histological hematoxylin and eosin (H&E) and Masson's trichrome staining was also used to assess the newly formed bone tissues. In H&E staining, the microgroove/PDMH–GP group presented the maximum woven bone structure on week 4 and lamellar bone structure on week 8 compared to other groups, indicating the most active osteogenesis process (Figure S5, Supporting Information). Notably, the Flat–Flat groups were mostly covered by fibrous connective tissues with little adjacent bone formation compared with other groups with adhesion surface patterns, indicating our proposed adhesion surface could effectively adhere to the bone and inhibit the soft tissue infiltration. We further performed the Masson's trichrome staining to assess the bone regeneration. More red staining indicating the mature lamellar bone could be found in the microgroove–GP and microgroove/PDMH–GP groups, while other groups showed more blue stained immature woven bone or osteoids (Figure S6, Supporting Information). We also used immunofluorescence staining of alpha smooth muscle actin (α-SMA) and OCN protein to investigate if the periosteum with anatomical patterns could promote the synchronous osteogenesis and angiogenesis. The α-SMA is enriched in vessel tissue and the OCN is identified as an essential marker for bone formation.[20] The neovasculature stained with α-SMA (red staining) were mostly located around the neighboring tissues of the newly formed bone (green staining).[21] In accordance with the in vitro qPCR results, the microgroove–GP and microgroove/PDMH–GP groups showed more α-SMA and OCN positive cells within the defect site compared to other groups, demonstrating their greater efficacy at promoting osteogenesis and angiogenesis (**Figure** 7A). Quantitatively, the microgroove/PDMH–GP groups presented 4.1 and 3.4 folds of blood vessel numbers and relative OCN intensity compared to the blank groups (Figure 7B,C). These promising results could be attributed to the biophysical cues of the anatomical patterned periosteum, due to the modulation of cell morphology and cell FA.[22] Taken together, through synchronous osteogenesis and angiogenesis enhancement, our Janus periosteum could lead to a more effective bone regeneration and provide auspicious prospect for the clinical treatment of bone fracture.

© 2021 Wiley-VCH GmbH

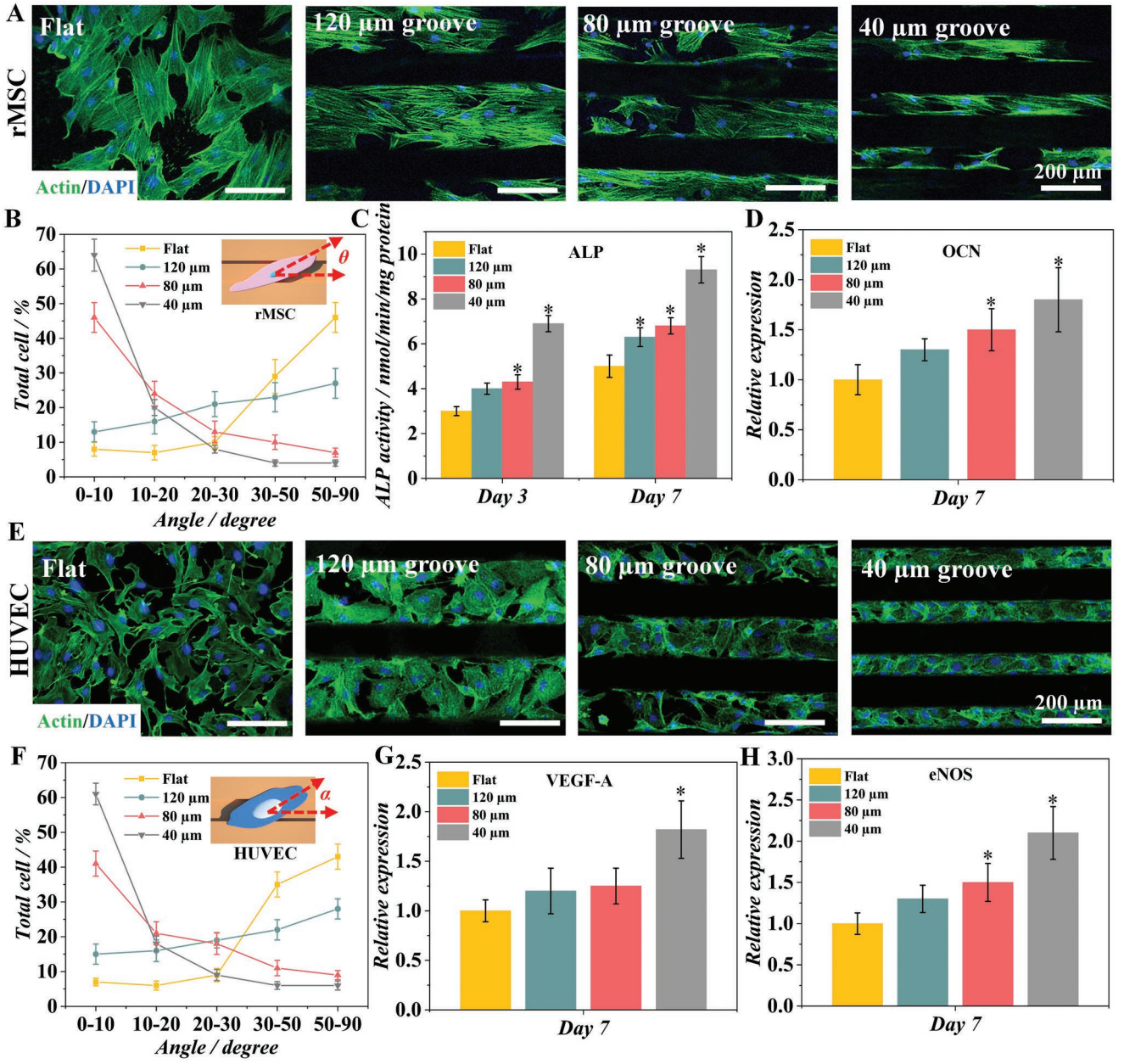

Figure 5. Cell alignment evaluation of the A) rMSC and E) HUVECs on the periosteum mimicking microgrooved patterns using actin/DAPI staining at day 3. Green and blue fluorescence indicates cell filaments and cell nuclei, respectively. Statistical analysis of cell alignment of B) rMSC and F) HUVECs. The inset images are the schematic of the quantification methods. C) ALP activity evaluation of the rMSC after 3 and 7 days of incubation and D) relative expression of the OCN gene. Relative expression of the angiogenetic G) VEGF-A and H) eNOS genes of the HUVECs. $^{*}p < 0.05$ compared with the flat surface group.

3. Conclusion

In summary, we have developed a bio-inspired Janus periosteum with anisotropic surface adhesion and anatomical pattern for bone regeneration. The resultant Janus periosteum is integrated with the fibrillar setae arrays of gecko feet, adhesive protein of mussel byssus, and the anatomical topographic microgrooved patterns of the natural periosteum. Such periosteum presented anisotropic adhesiveness with strong shear and normal adhesion in both dry and wet condition and effective cell modulation for synchronous osteogenesis and angiogenesis in vitro and in vivo. Our anisotropic periosteum with superior tissue adhesion and new bone and neovascular regeneration capacity demonstrated great potential for clinical regeneration of bone defects.

4. Experimental Section

Materials: PPG, LA, MAC, stannous octoate, HEMA, and phenylbis (2,4,6-trimethylbenzoyl) phosphine oxide (Irgacure 819) were purchased from Macklin reagent (Shanghai, China). DMA was purchased from Kaiwei

© 2021 Wiley-VCH GmbH

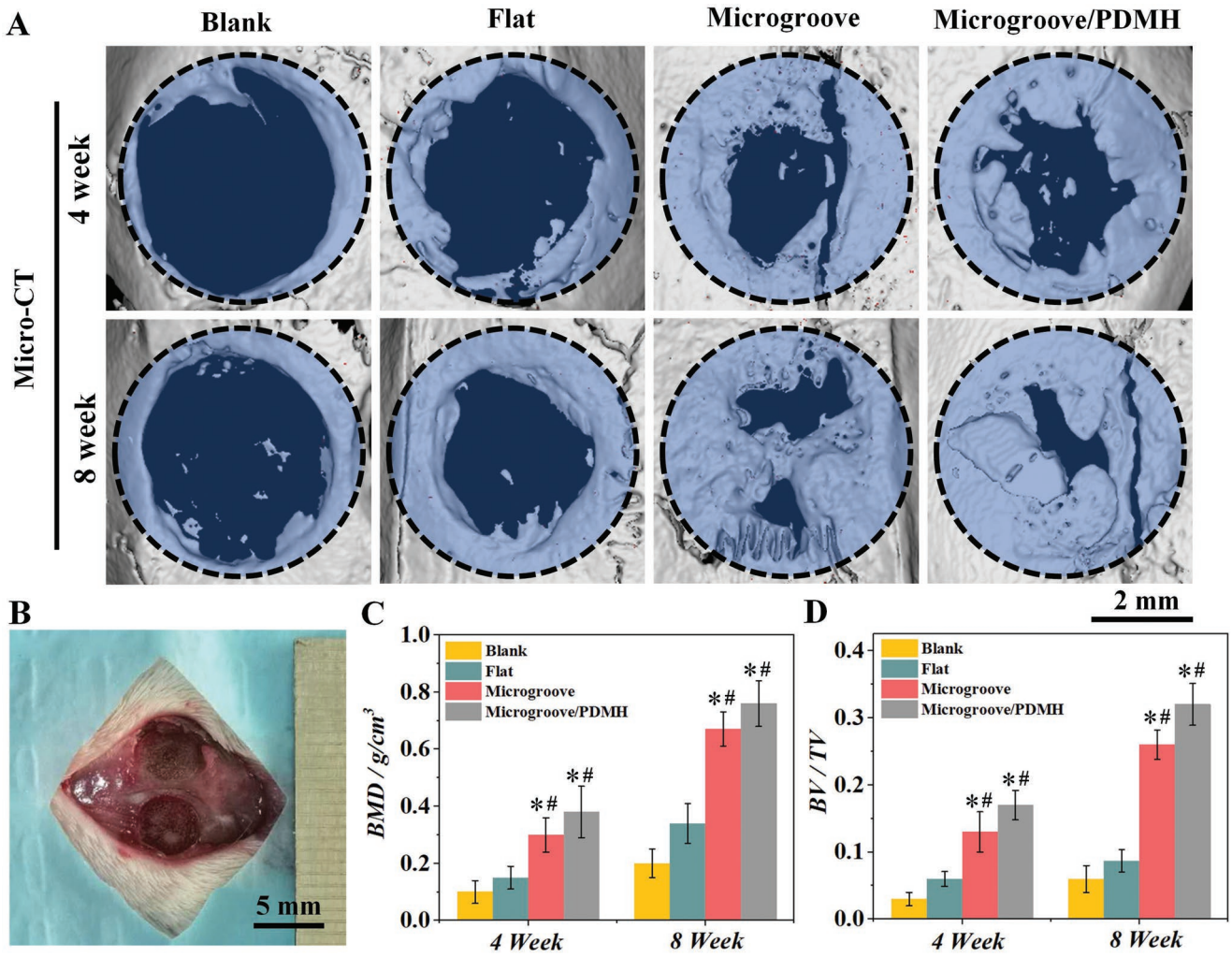

Figure 6. In vivo therapeutic performance of our Janus periosteum. A) Micro-CT reconstruction results presenting the new bone area of different experimental groups. B) Typical photograph of the established critical-sized calvarial defect model. Quantitative analysis of C) BMD and D) BV/TV 4- and 8-week post-operation. BMD: bone mineral density; BV/TV: bone volume/total volume. $^{*}p < 0.05$ compared with the Flat–Flat group and $^{\#}p < 0.05$ compared with the Flat–GP group.

chemical (Shanghai, China). Azobisisobutyronitrile, dimethylformamide (DMF), dimethyl sulfoxide, and methylene chloride was purchased from Sinopharm Chemical Reagent Co., Ltd. (Shanghai, China). rMSCs and HUVECs were purchased from Cyagen Inc. (Suzhou, China). Minimum Essential Medium α (α-MEM), osteogenic medium, endothelial cell medium (ECM), penicillin/streptomycin (PS), fetal bovine serum (FBS), and phosphate-buffered saline were all obtained from Gibco (USA). The Live/Dead assay kit, ALP activity assay, Alexa Fluor 488 Phalloidin, 4′, 6-diamidino-2-phenylindole (DAPI), and MTT Cell Proliferation Kit were purchased from the Thermo Fisher (USA). All other chemical reagents were purchased from Aladdin (Shanghai, China) if not specified.

Synthesis of PGLADMA: Photo-crosslinkable PGLADMA polymer was synthesized following the authors' previous protocol by a two-step reaction.[18a] Briefly, 40 g PPG and 23 g LA were mixed together and reacted for 6 h at 150 °C under nitrogen protection with stannous octoate as catalyst to obtain the PGLA. Then, methacrylate moieties were grafted to the PGLA chain by incorporation of 4.22 g methacryloyl chloride at 0 °C, both of which were diluted in dichloromethane. The product was purified by vacuum filtration after dissolving in diethyl ether and collected after rotary evaporation of the residual solvent. The attenuated total reflectance Fourier transform infrared (ATR-FTIR) (Bruker, US) was adopted to characterize the synthesized PGLADMA.

Synthesis of PDMH: The PDMH was synthesized according to previous study.[23] Briefly, the inhibitor of HEMA was first removed by basic alumina. Then, 1.7 mL HEMA, 0.62 g DMA, and 42 mg azobisisobutyronitrile were added to a round flask with 10 mL DMF. The mixture was bubbled with nitrogen for 30 min followed by co-polymerization at 60 °C. The resulting mixture was diluted by 10 mL methanol followed by dropwise adding into 150 mL diethyl ether to precipitate the synthesized PDMH copolymer. The purified co-polymer was thoroughly dried in a vacuum oven. ATR-FTIR was used to characterize the synthesized PDMH copolymer.

Fabrication of the Anisotropic Periosteum: The gecko inspired and natural periosteum mimicking polydimethylsiloxane (PDMS) negative molds were fabricated using standard microfabrication techniques by Nanzhi Institute of Advanced Optoelectronic Integration (Nanjing, China). The PGLADMA precrosslinking solution was prepared by thoroughly mixing 90 wt% PGLADMA, 9 wt% HEMA, and 1 wt% Irgacure 819 by the homogenizer. Then, the precrosslinked PGLADMA polymer was first placed between two PDMS negative molds with 250 µm interval. One PDMS mold was carved with fibrillar arrays (2 µm in diameter and 4 µm in height) and the other was carved with microgrooved patterns (40, 80, and 120 µm). The PGLADMA was then treated with vacuum to remove the trapped air, followed by photo-crosslinking with a UV lamp

© 2021 Wiley-VCH GmbH

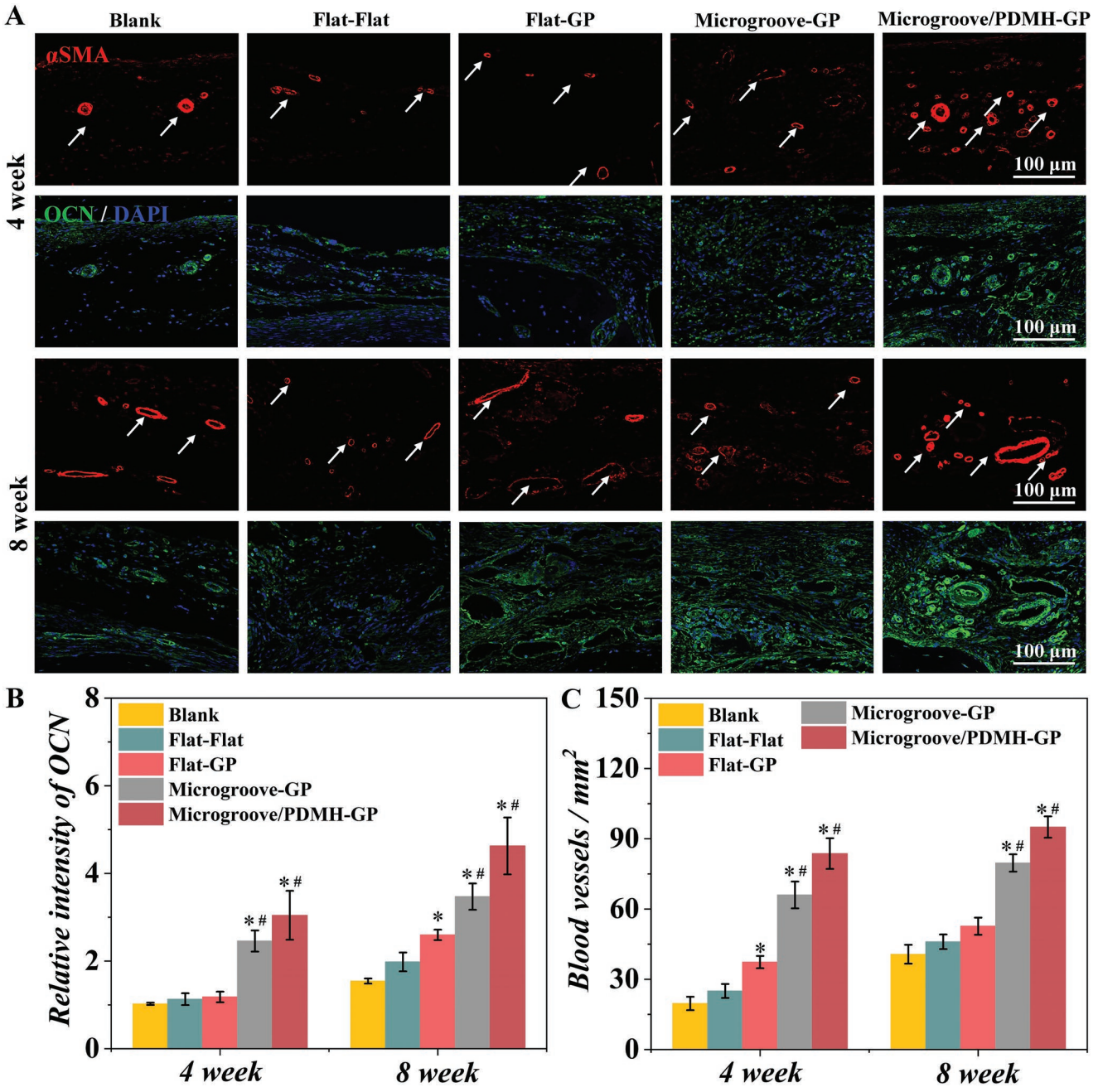

Figure 7. A) Immunofluorescence staining of α-SMA (red), OCN (green) protein, and DAPI (blue) in skull sections 4- and 8- week post-operation. The white arrows indicate the neo blood vessels. Quantification of B) blood vessel numbers and C) relative OCN intensity within the corresponding section. $^{*}p < 0.05$ compared with the Flat–Flat group and $^{\#}p < 0.05$ compared with the Flat–GP group.

(365 nm, 5 mW cm^{-2}) for 200 s to fully crosslink the PGLADMA. For the PDMH coated Janus periosteum, the PDMH was first dissolved in the ethanol with 1, 3, and 5 mg mL^{-1} concentration. Then, the prepared naked Janus periosteum was immersed in different concentration of the PDMH/ethanol solution for 2 h followed by the vacuum dry overnight at room temperature.

Tissue Adhesion Characterization: Both shear and normal tissue adhesion tests under dry and wet condition were performed based on previous protocol.[14] Briefly, a 10 mm × 10 mm porcine sausage skin membrane was glued to the glass slide and the other side of the porcine sausage skin was used for the adhesion test. Then, the fabricated anisotropic periosteum was cut into 10 mm × 10 mm and also glued to the glass slide. The surface with the gecko inspired pattern was used for the adhesion test. The shear and normal adhesion tests under dry condition were first performed. In the shear adhesion test, the prepared glass slides were placed together in the 10 mm × 10 mm area compressed with a constant 10 N force to establish a good contact with each other. Then, the two glass slides were pulled in parallel to the glass surface at a constant rate of 1 mm min^{-1} to measure the shear tissue adhesion strength. In the normal adhesion test, the tightly contacted glass slides were pulled perpendicularly to the glass surface at a constant rate of 1 mm min^{-1} to measure the normal tissue adhesion strength. To further

© 2021 Wiley-VCH GmbH

characterize the tissue adhesion behavior under wet condition, the wet adhesion test was also performed in which the two prepared slides were contacted and compressed under water. Then, the shear and normal tissue adhesion were measured following the previous protocol.

In Vitro Biocompatibility Characterization: The rMSCs were used to assess the cell viability, adhesion, and proliferation of the naked PGLADMA and the PDMH coated PGLADMA. Briefly, all the samples (10 mm in diameter) were sterilized and pre-soaked in culture medium for 24 h prior to cell seeding. Then, rMSCs were seeded onto the surface of the samples at 1×10^4 cells cm^{-2} and incubated for 1–3 days with α-MEM supplemented with 10% FBS and 1% PS in the incubator. At pre-determined time points, the Live/Dead assay kit and MTT Cell Proliferation Kit were adopted to characterize the cell viability and cell proliferation according to the manufacturer's protocol respectively. Further, cell morphology was tested by staining the intracellular filament *F*-actin by Alexa Fluor 488 Phalloidin and cell nuclei by DAPI according to the manufacturer's protocol. To calculate the cell spreading area, the stained *F*-actin fluorescent images were first converted into binary images using Image J software and then the surface coverage (indicates cell spreading area) of the binary images was quantified.[24]

In the protein absorption test, the fluorescein isothiocyanate labeled bovine serum albumin (FITC-BSA) was used as a model protein. Briefly, the different samples (10 mm in diameter) were immersed in the 0.5 mg mL^{-1} FITC-BSA solution for 12 h at 37 °C. Then, fluorescence microscope (Nikon, Japan) was used to detect the fluorescence signal of the samples. The fluorescence intensity from each sample was calculated using Image J software with background signal subtraction. Six randomly-chosen area (80 μm × 80 μm) was adopted for each experimental group.[25] In terms of the characterization of cell morphology and cytoskeleton organization, 1×10^4 cells cm^{-2} of the rMSCs or HUVECs was seeded onto the natural periosteum mimicking side of the anisotropic periosteum (10 mm in diameter) followed by 3 days of incubation. Then, the cell cytoskeleton organization was evaluated by the previous *F*-actin/DAPI staining. The cell orientation was calculated by measuring the cytoskeleton orientation angles using Image J software. The orientation angle was defined as the difference between the major cytoskeleton axis and the microgroove axis. Ten cells were selected for the calculation of each group.[26]

Osteogenesis and Angiogenesis Potential Assessment: The rMSCs were seeded onto the prepared periosteum mimicking side of the Janus periosteum (10 mm in diameter) with 5×10^4 cells cm^{-2} density. At pre-determined time points, ALP activity assay was used to quantify the ALP activity of rMSCs on different samples. In addition, the relative expressions of osteogenesis-related gene OCN were measured by qRT-PCR. Total RNA was extracted from rMSCs using Total RNA Kit (Omega, China) and was reverse transcribed into complementary DNA using the PrimeScript RT Master Mix Kit (Takarabio, China). GAPDH was used as an internal control for normalization. To evaluate the therapeutic efficacy of the anisotropic periosteum on angiogenesis, prepared samples (10 mm in diameter) were seeded with HUVECs with 5×10^4 cells cm^{-2} density and cultured using ECM. Then, the relative expressions of angiogenesis-related genes including VEGF-A and eNOS were quantified after 7 days of culture via the above-mentioned qRT-PCR protocol. The primer sequences are listed in Table S1, Supporting Information.

In Vivo Bone Regeneration Assessment: Male Sprague-Dawley rats aged 7–8 weeks and weighing 250–300 g were used to establish critical-sized calvarial defect model.[5,20,27] All animal procedures were performed in accordance with protocols approved by the Ethics Committee of the Affiliated Suzhou Hospital of Nanjing Medical University (K-2021-026). After anesthesia and disinfection, a longitudinal incision was created on the rat skull. Next, two bilateral critical-sized defects (5 mm in diameter) were made by dental trephine. The defects were filled with different Janus periosteum or left untreated. The wounds were closed with sutures and kept the rats individually in cages. After 4- and 8-week post-operation, the rats were sacrificed by CO_2 asphyxiation. Skull samples were harvested and fixed with 4% paraformaldehyde for the subsequent assessment. Micro-CT (SkyScan, Belgium) was adopted to characterize the 3D structure of the reconstructed bone tissue in the defect area with the settings of 65 kV, 385 mA, and 1 mm Al filter and the system software. BMD and BV/TV were quantitatively evaluated by CTAn software (Bruker, Belgium). Briefly, the reconstructed images were first imported into the CTAn software after calibration and set a circular region of interest (ROI) (consisting of 100 slices, 0.5 mm in diameter) to cover the defect sites. Then, the ROI was applied for the analysis of all samples and set the threshold values from 61 to 255. The BMD (g cm^{-3}) and BV/TV for the ROI was obtained by the software.[28] Then, the harvested calvaria samples were decalcified with 10% EDTA, embedded in paraffin, and sliced into 5 μm sections. The tissue sections were stained with H&E and Masson's trichrome staining to observe newly formed bone tissue. α-SMA and OCN immunofluorescence staining (Abcam, UK) was additionally performed to evaluate the formation of blood vessels.[29]

Statistical Analysis: All experiments were conducted in quadruplicate unless otherwise indicated. The data were presented as the mean ± standard deviation (SD). Statistical difference was analyzed using one-way analysis of variance followed by Tukey's multiple comparison test (SPSS Statistics, USA). p-value < 0.05 was considered statistically significant.

Supporting Information

Supporting Information is available from the Wiley Online Library or from the author.

Acknowledgements

Y.Y. and T.X. contributed equally to this work. This work was supported by the Start-Up Fund (1-ZE7S), Central Research Fund (G-YBWS), and Intra-Faculty Fund (ZVPC) from The Hong Kong Polytechnic University.

Conflict of Interest

The authors declare no conflict of interest.

Data Availability Statement

The data that support the findings of this study are available from the corresponding author upon reasonable request.

Keywords

anatomical pattern, bio-inspired surface textures, bone regeneration, Janus periosteum, tissue adhesion

Received: May 17, 2021
Revised: June 11, 2021
Published online:

[1] a) N. Li, J. Song, G. Zhu, X. Li, L. Liu, X. Shi, Y. Wang, *Biomater. Sci.* **2016**, *4*, 1554; b) Q. Wang, J. Xu, H. Jin, W. Zheng, X. Zhang, Y. Huang, Z. Qian, *Chin. Chem. Lett.* **2017**, *28*, 1801.
[2] Y. Zhou, F. Chen, S. T. Ho, M. A. Woodruff, T. M. Lim, D. W. Hutmacher, *Biomaterials* **2007**, *28*, 814.
[3] B. Schönmeyr, N. Clavin, T. Avraham, V. Longo, B. J. Mehrara, *Tissue Eng., Part A* **2009**, *15*, 1833.

© 2021 Wiley-VCH GmbH

[4] Y. Yang, T. Xu, Q. Zhang, Y. Piao, H. P. Bei, X. Zhao, *Small* **2021**, *17*, 2006598.
[5] L. Wu, Y. Gu, L. Liu, J. Tang, J. Mao, K. Xi, Z. Jiang, Y. Zhou, Y. Xu, L. Deng, *Biomaterials* **2020**, *227*, 119555.
[6] H. Y. Kim, J. H. Lee, H. A. R. Lee, J.-S. Park, D. K. Woo, H.-C. Lee, G.-J. Rho, J.-H. Byun, S. H. Oh, *ACS Appl. Mater. Interfaces* **2018**, *10*, 21091.
[7] a) Y. Yang, Q. Zhang, T. Xu, H. Zhang, M. Zhang, L. Lu, Y. Hao, J. H. Fuh, X. Zhao, *Biomaterials* **2020**, *263*, 120378; b) X. Zhao, I. Olsen, H. Li, K. Gellynck, P. G. Buxton, J. C. Knowles, V. Salih, A. M. Young, *Acta Biomater.* **2010**, *6*, 845; c) X. Zhao, I. Olsen, J. Pratten, J. C. Knowles, A. M. Young, *J. Mater. Sci.: Mater. Med.* **2011**, *22*, 1993.
[8] a) Y. Ma, S. Ma, Y. Wu, X. Pei, S. N. Gorb, Z. Wang, W. Liu, F. Zhou, *Adv. Mater.* **2018**, *30*, 1801595; b) H. K. Raut, A. Baji, H. H. Hariri, H. Parveen, G. S. Soh, H. Y. Low, K. L. Wood, *ACS Appl. Mater. Interfaces* **2018**, *10*, 1288; c) H. Shahsavan, S. M. Salili, A. Jákli, B. Zhao, *Adv. Mater.* **2017**, *29*, 1604021.
[9] a) M. Moffa, A. G. Sciancalepore, L. G. Passione, D. Pisignano, *Small* **2014**, *10*, 2439; b) H. Xu, H. Li, Q. Ke, J. Chang, *ACS Appl. Mater. Interfaces* **2015**, *7*, 8706; c) X. Shi, L. Li, S. Ostrovidov, Y. Shu, A. Khademhosseini, H. Wu, *ACS Appl. Mater. Interfaces* **2014**, *6*, 11915.
[10] a) D. Gan, T. Xu, W. Xing, M. Wang, J. Fang, K. Wang, X. Ge, C. W. Chan, F. Ren, H. Tan, X. Lu, *J. Mater. Chem. B* **2019**, *7*, 1716; b) A. R. Sasikala, A. GhavamiNejad, A. R. Unnithan, R. G. Thomas, M. Moon, Y. Y. Jeong, C. H. Park, C. S. Kim, *Nanoscale* **2015**, *7*, 18119.
[11] W. Zhang, R. Wang, Z. Sun, X. Zhu, Q. Zhao, T. Zhang, A. Cholewinski, F. K. Yang, B. Zhao, R. Pinnaratip, *Chem. Soc. Rev.* **2020**, *49*, 433.
[12] H. Yan, L. Li, Z. Wang, Y. Wang, M. Guo, X. Shi, J.-M. Yeh, P. Zhang, *ACS Biomater. Sci. Eng.* **2019**, *6*, 634.
[13] a) G. Huber, H. Mantz, R. Spolenak, K. Mecke, K. Jacobs, S. N. Gorb, E. Arzt, *Proc. Natl. Acad. Sci. U. S. A.* **2005**, *102*, 16293; b) T. E. Higham, A. P. Russell, P. H. Niewiarowski, A. Wright, T. Speck, *Integr. Comp. Biol.* **2019**, *59*, 148; c) P. Glass, H. Chung, N. R. Washburn, M. Sitti, *Langmuir* **2009**, *25*, 6607.
[14] a) A. Mahdavi, L. Ferreira, C. Sundback, J. W. Nichol, E. P. Chan, D. J. Carter, C. J. Bettinger, S. Patanavanich, L. Chignozha, E. Ben-Joseph, *Proc. Natl. Acad. Sci. U. S. A.* **2008**, *105*, 2307; b) B. Chen, G. Zhong, P. Goldberg Oppenheimer, C. Zhang, H. Tornatzky, S. Esconjauregui, S. Hofmann, J. Robertson, *ACS Appl. Mater. Interfaces* **2015**, *7*, 3626.
[15] H. Petite, V. Viateau, W. Bensaid, A. Meunier, C. de Pollak, M. Bourguignon, K. Oudina, L. Sedel, G. Guillemin, *Nat. Biotechnol.* **2000**, *18*, 959.
[16] X. Shi, T. Fujie, A. Saito, S. Takeoka, Y. Hou, Y. Shu, M. Chen, H. Wu, A. Khademhosseini, *Adv. Mater.* **2014**, *26*, 3290.
[17] A. Azeem, A. English, P. Kumar, A. Satyam, M. Biggs, E. Jones, B. Tripathi, N. Basu, J. Henkel, C. Vaquette, *Nanomedicine* **2015**, *10*, 693.
[18] a) Y. Yang, Q. Zhang, T. Xu, H. Zhang, M. Zhang, L. Lu, Y. Hao, J. H. Fuh, X. Zhao, *Biomaterials* **2020**, *263*, 120378; b) P. P. Spicer, J. D. Kretlow, S. Young, J. A. Jansen, F. K. Kasper, A. G. Mikos, *Nat. Protoc.* **2012**, *7*, 1918; c) S. Saha, X. B. Yang, N. Wijayathunga, S. Harris, G. A. Feichtinger, R. P. W. Davies, J. Kirkham, *Bone* **2019**, *127*, 602; d) W. Ji, F. Yang, J. Ma, M. J. Bouma, O. C. Boerman, Z. Chen, J. J. van den Beucken, J. A. Jansen, *Biomaterials* **2013**, *34*, 735.
[19] C. Renghini, V. Komlev, F. Fiori, E. Verné, F. Baino, C. Vitale-Brovarone, *Acta Biomater.* **2009**, *5*, 1328.
[20] T. Xin, J. Mao, L. Liu, J. Tang, L. Wu, X. Yu, Y. Gu, W. Cui, L. Chen, *ACS Appl. Mater. Interfaces* **2020**, *12*, 6840.
[21] G. Yang, H. Liu, Y. Cui, J. Li, X. Zhou, N. Wang, F. Wu, Y. Li, Y. Liu, X. Jiang, *Biomaterials* **2021**, *268*, 120561.
[22] a) Q. Wang, Y. Feng, M. He, W. Zhao, L. Qiu, C. Zhao, *Adv. Funct. Mater.* **2021**, *31*, 2008906; b) P. Viswanathan, M. G. Ondeck, S. Chirasatitsin, K. Ngamkham, G. C. Reilly, A. J. Engler, G. Battaglia, *Biomaterials* **2015**, *52*, 140.
[23] V. Jalaber, D. Del Frari, J. De Winter, K. Mehennaoui, S. Planchon, P. Choquet, C. Detrembleur, M. Moreno-Couranjou, *Front. Chem.* **2019**, *7*, 183.
[24] N. Gustafsson, S. Culley, G. Ashdown, D. M. Owen, P. M. Pereira, R. Henriques, *Nat. Commun.* **2016**, *7*, 12471.
[25] B. J. Yun, J. E. Kwon, K. Lee, W.-G. Koh, *Sens. Actuators, B* **2019**, *284*, 140.
[26] M. Zou, X. Zhao, X. Zhang, Y. Zhao, C. Zhang, K. Shi, *Chem. Eng. Sci.* **2020**, *398*, 125563.
[27] T. Xin, Y. Gu, R. Cheng, J. Tang, Z. Sun, W. Cui, L. Chen, *ACS Appl. Mater. Interfaces* **2017**, *9*, 41168.
[28] H. Gaêta-Araujo, E. H. L. Nascimento, D. M. Brasil, D. V. Madlum, F. Haiter-Neto, C. Oliveira-Santos, *Imaging Sci. Dent.* **2020**, *50*, 153.
[29] X. Sun, Q. Lang, H. Zhang, L. Cheng, Y. Zhang, G. Pan, X. Zhao, H. Yang, Y. Zhang, H. A. Santos, *Adv. Funct. Mater.* **2017**, *27*, 1604617.

© 2021 Wiley-VCH GmbH